ingegneria sismica
International Journal of Earthquake Engineering
Anno XLIII - Num. 3 - 2026

Comparative Analysis and Research on Finite Difference and Discrete Element of Slope in Diantan Open-pit Mine, Yunnan Province

Qianzhou Rong[1], *Shiguang Xu*[1,2,*], *Yi Yang*[1] *and Lichun He*[3]

[1] School of Public Safety and Emergency Management, Kunming University of Science and Technology, Kunming 650093, Yunnan, China
[2] Yunnan Geology and Mineral Engineering Investigation Group Corporation, Kunming 650041, Yunnan
[3] Hydrogeological Battalion of Jiangxi Geological Bureau, 330095, Nanchang, PRC

SUMMARY: *Slope stability has always been a key technical concern in the safe operation of open-pit mines. With the rapid advancement of computer technology, numerical simulation methods have increasingly replaced traditional qualitative approaches, providing a more quantitative means of analysis. This study focuses on the marble slope on the west side of the south mining pit at the Yunnan Diantan Iron Mine. Based on experimental data and parameter calculations, a three-dimensional model was constructed using Rhino software. Slope stability was then analyzed and compared using the three-dimensional finite difference method (FDM) via FLAC3D and the discrete element method (DEM) via 3DEC. The results indicate that the FDM simulation predominantly reveals features of typical push-pull or traction-type landslides, failing to capture the sudden, brittle failure often observed in rock collapses. In contrast, the DEM simulation better replicates the stepwise toppling behavior of rock slope failure, clearly demonstrating brittle fracture characteristics. Overall, DEM more effectively reflects the displacement and deformation behavior of rock slopes, produces less theoretical error, and yields simulation results that more closely align with actual mine conditions.*

KEYWORDS: *Open-pit mining, Stability analysis, Finite difference method (FDM), Discrete element method (DEM), Numerical simulation*

1 Introduction

With the continued deepening of open-pit mining, high and steep rock slopes have become a recurrent safety constraint in mine production. Recent three-dimensional numerical studies of open-pit slopes show that stability evaluation must account for slope geometry, in-situ stress redistribution, lithological heterogeneity and excavation-induced unloading rather than relying only on empirical judgment [1]. For the Diantan Iron Mine, these issues are amplified by the fractured marble mass, the steep upper benches and the fault-controlled weak zone near the pit bottom.

Conventional methods such as graphical analysis, kinematic assessment and the Slope Mass Rating (SMR) system remain useful for rapid screening, especially when field discontinuity data are limited. Their reliability decreases when the slope contains persistent joints, intersecting structural planes or local block separation, because these methods simplify the progressive mobilization of shear resistance and cannot directly reproduce discontinuity-

*hd4568921@sina.com
https://doi.org/10.65102/is20261256
Published: 10 June, 2026

controlled deformation [2]. Physical modelling studies have also shown that slope failure is highly sensitive to material structure, boundary restraint and loading path, which makes purely qualitative assessment insufficient for fractured rock slopes [3].

Numerical modelling therefore provides a more suitable basis for comparing the mechanical response of the Diantan slope. The finite difference method (FDM), as implemented in FLAC3D, represents the rock mass as an equivalent continuum and is efficient for calculating stress redistribution, plastic zones and overall factors of safety. The discrete element method (DEM), as implemented in 3DEC, treats the slope as interacting blocks separated by joints, which allows sliding, opening, rotation and block detachment to be simulated explicitly. Recent jointed-slope analyses based on DFN-DEM frameworks indicate that discontinuity geometry can strongly control the computed stability state and the final failure path [4]. Combined finite-discrete studies further show that continuum and discontinuum formulations may produce different deformation modes even under comparable geological conditions [5, 6].

Previous numerical studies have improved the simulation of rock-slope deformation, runout and progressive collapse; however, many applications still emphasize a single stability coefficient rather than comparing whether different modelling assumptions reproduce the observed failure mechanism. DEM analysis of bonded granular slopes has demonstrated the importance of block interaction and contact degradation [7], while continuum-discontinuum modelling of rockslide runout has shown that progressive failure cannot be fully described by a single continuum response [8]. This provides the basis for a direct FDM-DEM comparison under the same geological setting.

This study uses the west slope of the south pit at the Yunnan Diantan Iron Mine as a field case. Laboratory and field-test parameters are used to construct a three-dimensional geological model in Rhino, followed by FDM simulation in FLAC3D and DEM simulation in 3DEC. The comparison focuses on three verifiable outputs: factor of safety, displacement components and failure-mode reproduction. The objective is to determine which modelling strategy better reflects the deformation behaviour of a jointed marble slope under natural and rainfall-weakened conditions.

2 Geological and Structural Characteristics of the Study Slope

2.1 Regional Setting and Lithological Overview

The study area is located on the west side of the south pit at the Diantan Iron Mine, situated in Yunnan Province, southwestern China (see Figure 1). The site is characterized by relatively simple lithological composition. The predominant formation exposed on the eastern slope area is the Upper Carboniferous Kongshuhe Formation (Ck2), which is structurally controlled by local faulting.

Figure 1: Geographic location of the Diantan Iron Mine in Yunnan Province, southwestern China

The slope under investigation is approximately 200 meters long along its strike, with a vertical height difference of about 55 meters. The step slope angle ranges from 27° to 78°, while the final overall slope angle is between 32° and 35°, as illustrated in Figure 2. A working platform approximately 50 meters wide is located at an elevation of 1850 meters. Above the platform are two steep benches, with slope angles between 50° and 78° and step heights ranging from 15 to 47 meters. These upper benches are heavily jointed, with visible surface cracks approximately 1 cm wide near the southern edge. Below the platform, there are four additional benches with gentler slopes (27°–40°) and step heights between 5 and 18 meters. Near the pit bottom, a fault zone approximately 5 to 13 meters wide is present. This zone features highly fractured and fragmented rock masses with well-developed fissures filled with mud, making the slope surface prone to localized rockfalls.

According to borehole data from both historical exploration and newly drilled holes, the west slope is primarily composed of strongly weathered marble. The uppermost layer includes a fully weathered marble zone and a Quaternary overburden, both approximately 1.6 meters thick and mostly removed during excavation. Beneath this lies a moderately weathered skarn unit, separated from the marble by a fractured structural contact. The southwest-facing open pit crest serves as a haulage route and drainage outlet for pit dewatering.

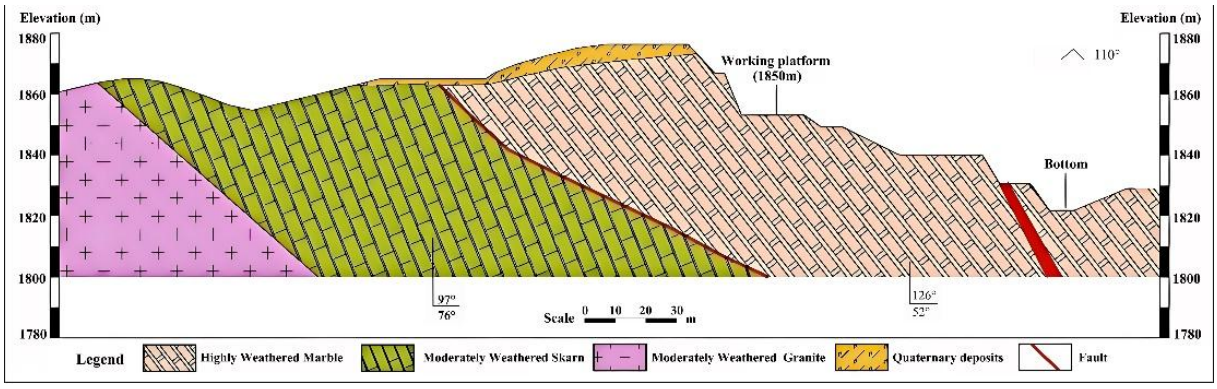

Figure 2: Typical profile of the west side of the South mining pit of Diantan Iron Mine.

2.2 Structural Features and Discontinuity Analysis

Field mapping and structural measurements revealed four dominant sets of discontinuities in the west slope area:

Set J1 (bedding planes): Orientation 110°/60°, dipping southeast; spacing approximately 2 joints per meter. These planes are continuous and tightly closed. Set J2: Orientation 032°/52°, dipping northeast; spacing approximately 3 joints per meter. The joint surfaces are well-closed and persistent. Set J3: Orientation 166°/44°, dipping northeast; spacing approximately 3 joints per meter. These joints are slightly open, with an average aperture of about 1.1 mm. Set J4: Orientation 250°/37°, dipping southwest; spacing approximately 1 joint per meter.

Figure 3 presents a stereographic (lower hemisphere, equal-angle) projection showing the orientations of the slope face and major joint sets. The west slope is classified as a forward-dipping slope, in which the dip angle of the strata generally exceeds the slope angle. As a result, bedding planes (J1) are not favorably oriented for planar sliding and are therefore less likely to induce instability. Similarly, Set J4 dips into the slope, indicating low potential for failure along this set.

In contrast, joint sets J2 and J3 intersect the slope face at oblique angles, creating wedge-shaped rock masses with inclinations greater than the slope angle. This geometric configuration increases the likelihood of planar and wedge-type failures. Based on their orientations and spacing, sets J1, J2, and J3 are identified as the main unfavorable structural planes affecting slope stability. Due to the steep dip angles and intersecting nature of these joints, failure along pre-existing structural planes is considered the most probable failure mechanism for this slope.

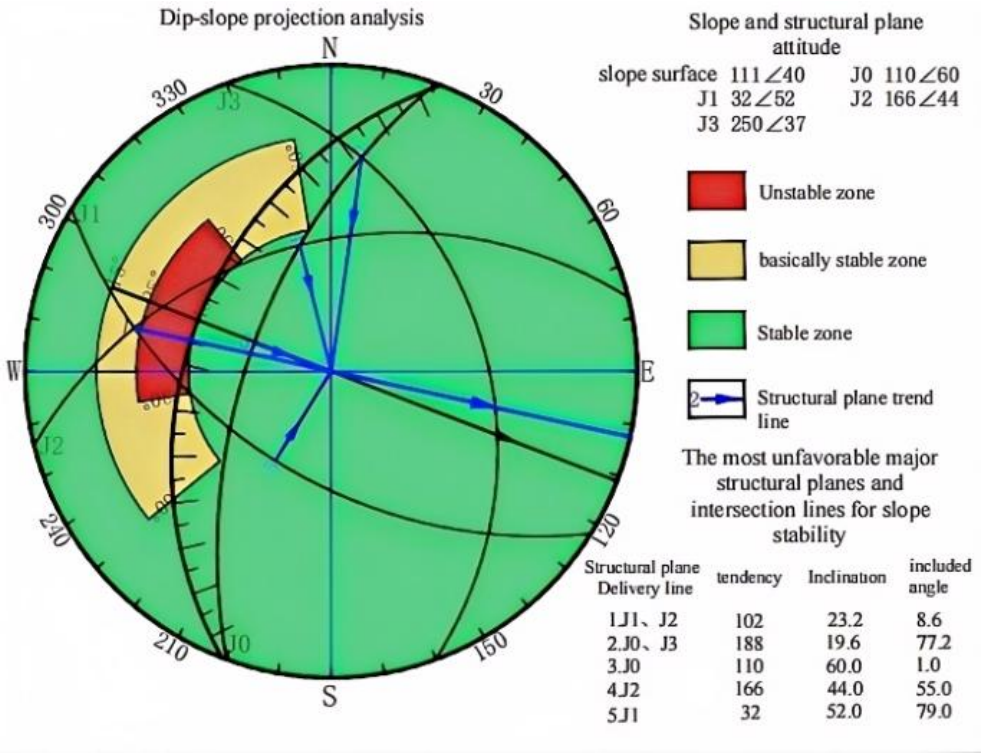

Figure 3: Stereographic projection (lower hemisphere, equal angle) showing orientations of major joint sets and slope face in the west slope area.

3 Determination of Rock Mass and Structural Plane Parameters

Accurate selection of mechanical parameters for both rock blocks and structural planes is critical to the reliability of numerical simulation. This section reports the laboratory point-load tests, uniaxial compressive strength tests, in-situ shear tests and empirical conversions used to

determine the strength and deformation parameters of the studied rock mass. Laboratory testing followed the ISRM suggested methods for rock characterization, testing and monitoring [9]. Specimens were prepared with an approximate length-to-diameter ratio of 2.5. Point-load tests were conducted using a YAW-300 testing machine under ambient temperature of 22–25°C and relative humidity below 60%.

3.1 Laboratory and In-situ Testing of Rock Mass Strength

3.1.1 Point Load Strength Test

To characterize the uniaxial strength of different rock types present in the slope, point load tests were performed on samples collected from boreholes distributed across the study area. The dominant lithologies include strongly weathered marble, moderately weathered skarn, and fault breccia zones. A total of 79 samples of strongly weathered marble, 24 samples of moderately weathered skarn, and 15 samples from fault breccia zones were tested. The point load index provides an estimate of the uniaxial compressive strength (UCS) of the rock based on established conversion relationships. The average point load strength values of each rock type obtained through the collation and analysis of the data are shown in Table 1.

Table 1: Point load results table

Lithology	Type	Average (MPa)	Standard deviation	Variation coefficient	Statistical correction coefficient	Standard values (MPa)
Strongly weathered marble	Compressive resistance	38.73	21.89	0.57	0.9084	35.18
Moderately weathered skarn	Tensile strength	8.19	6.01	0.73	0.7194	5.90
	Compressive resistance	108.32	62.47	0.58	0.7795	84.44
Fault fracture zone	Compressive resistance	26.79	23.52	0.88	0.8902	23.85
	Tensile strength	1.38	1.55	1.13	0.859	1.182

3.1.2 In-situ Direct Shear Test

In-situ direct shear tests were conducted within boreholes to evaluate the shear strength of the rock mass under natural confinement. This test method is preferred over laboratory-based shear tests as it minimizes the influence of sampling disturbance, such as water loss or structural changes. Shear tests were mainly performed on strongly weathered marble and the rock mass within the fault zone at varying depths. The tests yielded cohesion (c) and internal friction angle (φ) parameters by fitting the shear strength envelope from Mohr-Coulomb theory. The results are shown in Table 2 below

Table 2: Direct shear results in holes

Lithology	Saturation density (kg/m^3)	Internal friction angle (°)	Cohesive force (KPa)	Residual internal friction angle (°)
Strongly weathered marble	2686	25.8	40.1	17.3
Fault fracture zone	2310	17.8	26.7	13.72

3.2 Rock Mass Strength Estimation Based on GSI

Because microcracks and small-scale discontinuities cannot be fully represented by laboratory tests alone, the Geological Strength Index (GSI) approach was used to estimate equivalent mechanical parameters for rock blocks without dominant structural planes. The Hoek-Brown criterion was adopted to convert lithological condition, weathering degree and joint condition into rock-mass strength parameters [10]. GSI values were determined from outcrop observations and borehole-wall descriptions. Strongly weathered marble with open and continuous joints was classified as blocky/disturbed, with GSI values of 30–35. Moderately weathered skarn with better interlocking and fewer joints was classified as very blocky, with GSI values of 45–50. The following parameters are required to compute the mechanical properties using the Hoek-Brown criterion:

$$\sigma_1 = \sigma_3 + \sigma_c (m_b \frac{\sigma_3}{\sigma_c} + s) \tag{1}$$

$$m_b = m_i \exp(\frac{GSI - 100}{28 - 14D}) \tag{2}$$

$$s = \exp(\frac{GSI - 100}{9 - 3D}) \tag{3}$$

In the above formula, σci is the uniaxial compressive strength derived from point-load conversion, mi is the lithology-dependent material constant, and D is the disturbance factor. A value of D = 0.7 was used for the mechanically excavated slope according to the Hoek-Brown disturbance-factor recommendation [11]. The sensitivity analysis in Section 5 indicates that changing D between 0.5 and 1.0 produces less than 10% variation in the derived shear-strength parameters.

Using the Hoek-Brown criterion and the derived GSI values, the equivalent Mohr-Coulomb parameters (cohesion *c* and internal friction angle *φ*) were obtained through regression analysis over a stress range, as recommended by Hoek and Brown (1997). The Mohr–Coulomb parameters are calculated using the following relationships:

$$\phi = \sin^{-1}[\frac{6am_b\left(s + m_b\sigma_{3n}\right)^{a-1}}{2(1+a)(2+a) + 6am_b\left(s + m_b\sigma_{3n}\right)^{a-1}}] \tag{4}$$

$$c = \frac{\sigma_c[(1+2a)s + (1-a)m_b\sigma_{3n}](s + m_b\sigma_{3n})^{a-1}}{(1-a)(2+a)\sqrt{1 + [6am_b(s + m_b\sigma_{3n})^{a-1}]/[(1+a)(2+a)]}} \tag{5}$$

where σ is the upper limit of the minimum principal stress interval for the relationship between the Mohr-Coulomb criterion and the Hoek-Brown criterion, as determined by following Equations:

$$\sigma_{3\max} = 0.47\sigma_{cm}(\frac{\sigma_{cm}}{\gamma H})^{-0.94} \tag{6}$$

$$\sigma_{cm} = \sigma_c \frac{[m_b + 4s - a(m_b - 8s)](m_b / 4 + s)^{a-1}}{2(1+a)(2+a)} \tag{7}$$

where H represents the height of the slope and σ_{cm} is the overall strength of the rock mass. The parameters of the shear strength of the rock mass obtained based on geological strength indicators are shown in Table 3.

Table 3: Values of geological strength index parameters

Rock name	GSI value	m_i	Cohesion c (MPa)	Internal friction Angle φ(°)
Strongly weathered marble	32	10	0.093	40.1
Fault fracture zone	23	7	0.031	34.2
Medium weathered skarn	46	13	0.219	56.72

3.3 Determination of Structural Plane Parameters

The mechanical parameters of structural planes, including normal stiffness, shear stiffness, cohesion and friction angle, were determined from laboratory testing, in-situ information and empirical estimation. Because representative joint samples are difficult to prepare and in-situ joint testing is sensitive to disturbance, empirical stiffness estimation was used where direct measurements were unavailable. The Barton-Bandis framework relates joint normal and shear stiffness to joint roughness, wall strength and contact condition, and is therefore suitable for parameterizing discontinuities in block-based numerical models [12].

3.3.1 JCS Determination Method

JCS refers to the compressive strength of the rock on both sides of the structural plane. In this study, JCS values were estimated from point load test results conducted on representative rock samples. The values obtained for each lithology are summarized in Table 4. Note that due to limitations in sampling quantity and quality—particularly the lack of paired samples from both sides of a joint—the JCS values presented here are approximate. The point load-derived UCS values may not fully capture the localized strength variations of joint walls.

Table 4: Estimated JCS values for different structural plane lithologies

Structural plane lithology	JCS (MPa)
Strongly weathered marble	35.18
Fault fracture zone	23.85

3.3.2 JRC Determination Method

The Joint Roughness Coefficient (JRC) is a key parameter for evaluating the shear strength of rock joints. In this study, two methods were used to estimate JRC values for representative structural planes: visual comparison using Barton's standard roughness profiles and quantitative derivation based on the Z^2 method.

Barton proposed standard roughness profiles derived from direct shear tests on natural joint surfaces, linking visual surface morphology to JRC values [13]. In field application, each joint surface is compared with the standard profiles and assigned a representative JRC. To reduce observer subjectivity, the Z^2 method proposed by Tse and Cruden was also used to calculate JRC from digitized joint profiles [14].

$$JRC=32.2+32.47\log Z_2 \tag{8}$$

$$Z_2=\frac{1}{L}\sqrt{\int_{x=0}^{x=L}\left(\frac{dy}{dx}\right)^2} \tag{9}$$

where L is the projected length of the joint profile in the horizontal (x) direction; Z is the root mean square of the slope across the profile.

Yau et al. showed that calculated Z^2 values are sensitive to sampling resolution; therefore, a 1.27 mm sampling interval was adopted to remain consistent with the original calibration [15]. Joint profiles were digitized from high-resolution fracture scanline images, and RMS slope values were calculated at uniform intervals using OriginLab. Barton's standard profiles were also reconstructed for comparison and validation of the Z^2 method.

As shown in Table 5, the values calculated using the Z^2 method at a 1.27 mm interval show good agreement with Barton's standard values, validating the accuracy and reliability of the approach. Using the Z^2 method, a total of 33 joint profiles from strongly weathered marble and 9 profiles from the fault fracture zone were analyzed. The distribution of calculated JRC values is presented in Figure 4.

Table 5: Comparison of JRC calculation values

Barton Curve numbering	Barton Standard values	The root mean square calculated value	Barton Curve numbering	Barton Standard values	Root mean square calculated value
1	0.4	0.6	6	10.8	10.7
2	2.8	3.0	7	12.8	12.5
3	5.8	5.9	8	14.5	14.8
4	6.7	6.7	9	16.7	16.9
5	9.5	9.6	10	18.7	18.6

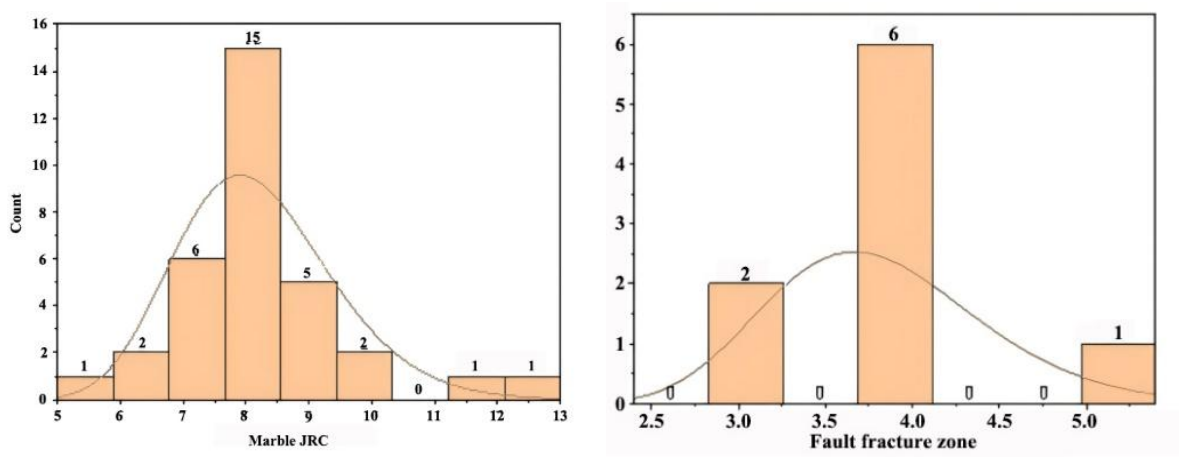

(a) (b)

Figure 4: (a) Distribution map of JRC in marble; (b) Distribution map of JRC in fault fracture zone.

According to the analysis, the JRC values for strongly weathered marble range primarily between 7.7 and 8.6, with a representative average value of 7.9. In contrast, the JRC values for joints in the fault fracture zone range from 3.4 to 4.2, with a representative average of 3.6.

3.4 Determination of Joint Stiffness and Shear Strength Parameters

3.4.1 Fundamental Understanding of Joint Stiffness

According to Goodman, normal stiffness is the gradient of normal stress required to generate deformation in the normal direction of a discontinuity [16]. It is controlled by the mechanical properties of the surrounding rock, the number and area of contact points, surface morphology and the degree of interlocking. Joint stiffness is theoretically stress-dependent rather than constant, especially under changing confinement. The mathematical expression is given by:

$$K_{\mathrm{n}} = \frac{\sigma_{\mathrm{n}}}{\mu_{\mathrm{n}}} \tag{10}$$

where K_{n} is the normal stiffness (MPa/m), σ_{n} is the normal compressive stress (MPa), μ_{n} is the corresponding normal displacement (m).

Similarly, the shear stiffness (also referred to as tangential stiffness) is defined as the gradient of shear stress required to induce tangential deformation. Experimental studies have shown that for relatively hard joint surfaces, shear stiffness tends to remain approximately constant. However, for weaker or partially filled joints, shear stiffness may vary significantly with changes in normal stress.

$$K_{\mathrm{s}} = \frac{\sigma_{\mathrm{s}}}{\mu_{\mathrm{s}}} \tag{11}$$

where K_{s} is the shear stiffness (MPa/m), σ_{s} is the shear compressive stress (MPa), μ_{s} is the corresponding shear displacement (m).

3.4.2 Empirical Estimation of Joint Stiffness

The empirical stiffness relationships used here estimate joint stiffness from joint roughness coefficient (JRC), joint wall compressive strength (JCS), trace length and residual friction angle. These relationships incorporate site-specific joint geometry and were applied to obtain the stiffness parameters listed in Table 6.

$$K_{\mathrm{n}} = -7.15 + 1.75JRC + 2\left(\frac{JCS}{JRC}\right) \tag{12}$$

$$K_{\mathrm{s}} = \frac{JRC \cdot JCS}{L} \cdot \tan\phi_r \tag{13}$$

where K_{n} is the normal stiffness (MPa/m), JRC is the joint roughness coefficient, JCS is the compressive strength of the joint wall (MPa), K_{s} is the normal stiffness (MPa/m), L is the trace length of the joint (mm), ϕ_r is the residual friction angle.

For joints containing gouge or infill materials, stiffness may be significantly reduced. In such cases, the degree of joint aperture is a key factor. If the joint is tightly closed, its mechanical behavior resembles that of a clean joint. Conversely, if the joint is widely open, its stiffness is largely controlled by the mechanical properties of the infilling material, which should be determined through laboratory testing. The calculated values of normal and shear stiffness for

representative structural planes, including strongly weathered marble and fault fracture zones, are summarized in Table 6.

Table 6: Comparison of JRC calculation values

Structural planes Types	Trace length L (mm)	JRC	JCS	Residual friction angle (°)	K_n (GPa/m)	K_s (GPa/m)
Marble Structural planes	1200	7.9	35.18	15.3	15.58	0.80
Fault fracture zone structural plane	2100	3.6	23.85	13.72	12.4	0.28

3.4.3 Determination of Shear Strength Parameters

The shear strength of rock joints was described using Barton's nonlinear shear strength criterion, which is commonly used for rough natural discontinuities under low-to-moderate normal stress [17]. The criterion is expressed as:

$$\tau = \sigma_n \cdot \tan\left(JRC \cdot \log_{10}\left(\frac{JCS}{\sigma_n} \right) + \phi_b \right) \tag{14}$$

where τ is the peak shear strength (MPa), σ_n is the applied normal stress (MPa), ϕ_b is the basic friction angle.

Although Barton's criterion provides a more realistic representation of joint behavior under low-to-moderate stress levels, its applicability under high normal stress may be limited due to increasing nonlinear error. Furthermore, most numerical simulation software (e.g., 3DEC) adopts the linear Mohr-Coulomb criterion, which necessitates transforming Barton's nonlinear envelope into equivalent cohesion and internal friction angle. To achieve this transformation, shear strength values were computed from Equation (14) under a range of applied normal stresses. These data points were then subjected to regression analysis to fit a linear Mohr-Coulomb envelope:

$$\tau = c + \sigma_n \cdot \tan\phi \tag{15}$$

Specifically, shear strength values (τ) are computed using the Barton formula under a range of assumed normal stress conditions (σ). The procedure involves selecting a series of normal stress values, applying the Barton equation to compute the corresponding shear strengths, and compiling these values into a dataset. By plotting the calculated shear strength (τ) against the normal stress (σ), a linear regression can be performed. In this linear fit, the intercept with the shear strength axis represents the cohesive strength (c), and the slope of the regression line corresponds to the tangent of the internal friction angle (tanφ). The derived linear relationship can then be interpreted within the Mohr–Coulomb framework, thus enabling compatibility between empirical data and numerical modeling approaches. Figure 5 shows the regression fitting results for two representative cases: strongly weathered marble and a fault fracture zone, respectively. Based on these regression analyses, the estimated values of cohesion and internal friction angle for each structural plane type are summarized in Table 7.

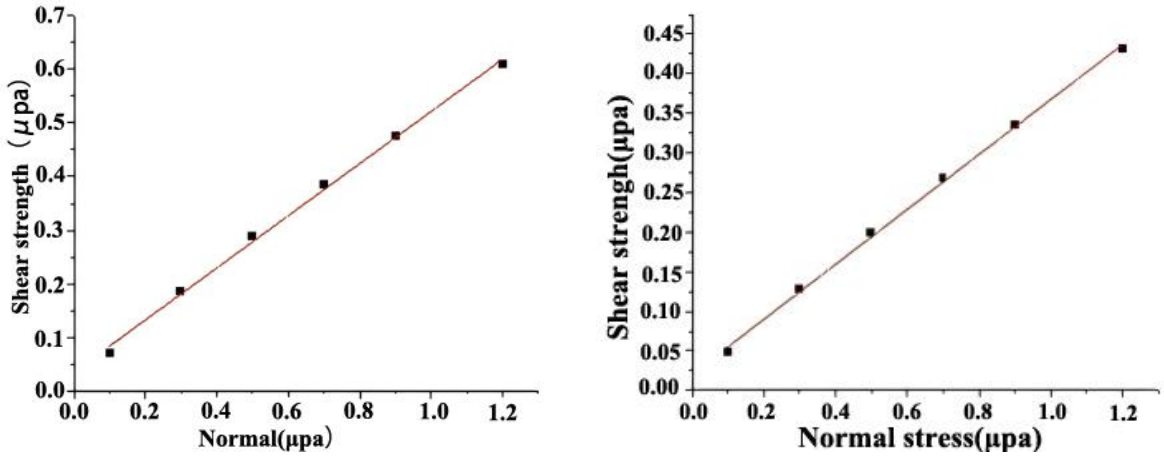

(a) (b)

Figure 5: (a) Fitting curve of strongly weathered marble; (b) Fitting curve of fault fracture zone.

Table 7: Estimated Mohr–Coulomb strength parameters derived from the Barton formula.

Structural planes Types	K_n (GPa/m)	K_s (GPa/m)
Strongly weathered marble	35.3	25.6
Fault fracture zone	20.7	18.9

4 Slope Stability Analysis

4.1 External Geological Modeling of the Study Area

To accurately simulate slope deformation and failure in the study area, a high-fidelity three-dimensional geological model was constructed by integrating topographic, geological, and structural data. The mining area is characterized by a series of artificially excavated slopes and intersecting road networks, resulting in terrain that is more akin to engineered planar surfaces than natural landforms. To reflect these anthropogenic geometries, Rhino software was employed to construct surface models based on topographic survey data (Figure 6a). The external boundaries of the model (Figure 6b) were defined to fully enclose the slope body and its surrounding influence zone.

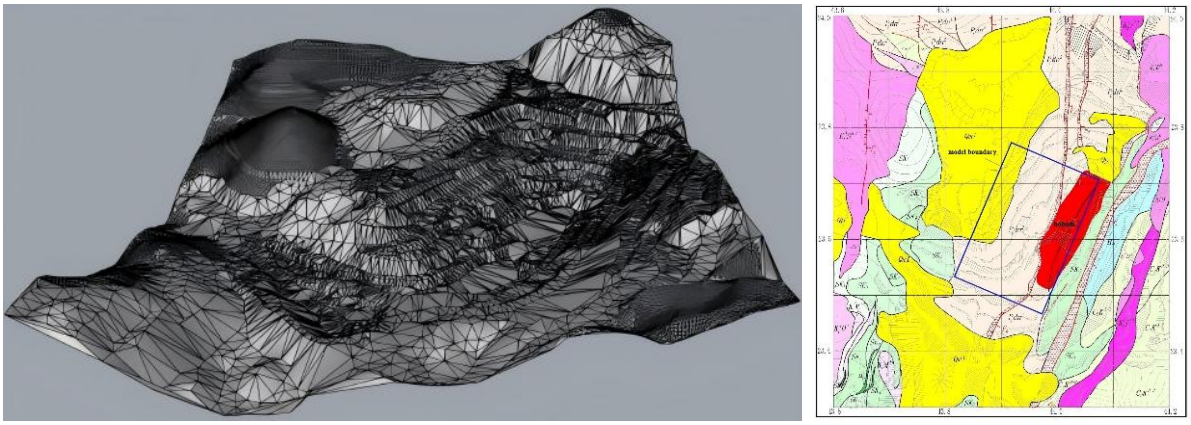

(a) (b)

Figure 6: (a) Surface model of the study area constructed using Rhino; (b) Defined external boundary of the simulation model.

The stratigraphy in the study area mainly comprises marble, skarn, and residual Quaternary deposits. Due to prolonged excavation, most of the Quaternary cover and completely weathered layers at the slope crest have been removed or are negligibly thin; hence, they were excluded from the model. The skarn units, located at the base of the slope, were lithologically diverse but mechanically similar, and were thus treated as a unified rock mass for modeling purposes. The final 3D surface model is shown in Figure 7a.This surface model was then imported into the 3DEC numerical simulation platform for discrete element analysis. Within 3DEC, the geometry was regrouped and merged to form a solid block model (Figure 7b). To capture the mechanical behavior of discontinuous rock masses, a network of structural planes was implemented to segment the model into polyhedral blocks.

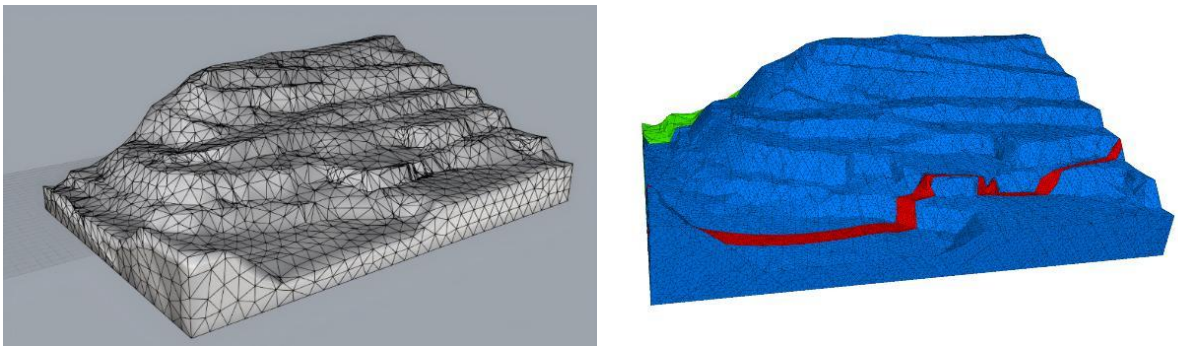

(a) (b)

Figure 7: (a) Finalized geological 3D model; (b) Block model imported into 3DEC.

The overall model dimensions are approximately 240m (length) × 160m (width) × 80m (height). This scale ensures that both the entire slope and its mechanical influence zone are fully included, avoiding artificial boundary effects. The model was discretized into zones ranging from 1.0 to 3.0 meters, with finer zones applied near structural planes and areas of expected failure. The total number of zones in the final model exceeds 200,000, which provides adequate resolution for detailed mechanical response analysis while maintaining computational efficiency. Boundary conditions were set as follows:

Bottom boundary: fixed in all directions to simulate bedrock confinement. Lateral boundaries: roller constraints (displacement restricted normal to boundary but free in the tangential direction).

Top surface: free, with gravity loading applied uniformly to represent the self-weight of the rock mass. Seepage and mechanical effects of rainfall were included in subsequent analyses by adjusting material properties.

The rock mass contains a complex system of discontinuities, as observed from extensive field surveys. To represent the most influential joint sets while maintaining computational feasibility, only the dominant discontinuities were modeled. These included three unfavorable joint sets based on stereographic projection and engineering relevance: J1 (bedding planes): orientation 110°/60°, dipping southeast, spacing ~10 m, persistence 100%; J2: orientation 32°/52°, dipping northeast, spacing ~4 m, persistence 40%; J3: orientation 166°/44°, dipping northeast, spacing ~4 m, persistence 40%.

These joints were implemented using the jset command in the FISH scripting language of 3DEC, allowing precise control of dip, dip direction, spacing, and continuity. In addition, the highly fractured fault zone at the toe of the slope was represented using the densify command to generate fragmented rock blocks with maximum dimensions less than 1.0 m (Figure 8), capturing the mechanical weakening associated with faulting.

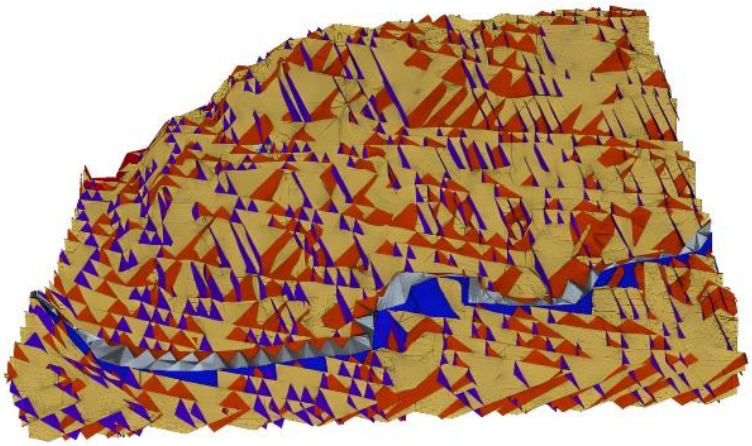

Figure 8: Structural plane network applied to segment the rock mass.

Each lithological layer was assigned material properties derived from laboratory tests and field classifications (Table 8). The model assumes linear elastic behavior before failure and uses the Mohr-Coulomb strength criterion for both intact blocks and discontinuities. Joint stiffness and strength parameters were obtained from the Barton-Bandis empirical framework, using JRC values derived from digital image analysis of surface photographs. The factor of safety (FoS) was calculated through the strength reduction method (SRM), in which cohesion and friction angle are progressively reduced until numerical non-convergence or rapid displacement growth indicates incipient failure.

Table 8: Comparison of JRC calculation values

Lithology	Density	Cohesion (kPa)	Friction angle (°)	E (GPa)	Poisson's ratio	K_n (GPa/m)	K_s (GPa/m)
Marble	2620	46.3	28.2	9.12	0.28	15.58	0.8
Fault	2200	31.2	20.7	2.2	0.34	12.4	0.28
Skarca	2524	219	56.72	26.5	0.22	/	/

4.2 Discrete Element Simulation and Stability Analysis

To investigate the slope stability and failure mechanisms under both natural and extreme weather conditions, numerical simulations were conducted using the Discrete Element Method (DEM) implemented in 3DEC. In this approach, the rock mass is represented as an assemblage of discrete blocks separated by discontinuities, allowing for the explicit modeling of joint deformation, block interaction, and potential detachment under loading.

Figures 9 shows the displacement cloud maps under natural (dry) conditions. The analysis indicates that the overall slope remains stable, with a calculated Factor of Safety (FoS) of 1.33, which exceeds the typical stability threshold of 1.1–1.2 for open-pit mining slopes, implying no imminent failure under self-weight loading. Displacement is concentrated at the upper eastern slope, near the free surface. The peak total displacement reached 0.44 cm, and directional components were: The X-direction displacement peaks at 0.29 cm, occurring near the upper slope fissures aligned with unfavorable joint set J2. This suggests potential shear-induced relative movement along these discontinuities. The localized nature of this movement indicates that joint sliding, rather than block translation or rotation, is the dominant mechanism.; The Y-direction displacement, reaching -0.24 cm, is primarily concentrated on the southern slope surface. This lateral movement may be associated with differential stiffness and joint orientations, which allow for horizontal dilation or flexure of rock blocks in response to

gravitational loading; The Z-direction displacement, with a maximum of -0.41 cm, reflects vertical settlement at the top of the slope and minor uplift near the slope toe. This is likely due to joint compression and minor block rearrangement, consistent with the mechanical behavior of jointed rock masses under vertical stress. Displacements are mainly concentrated at the upper eastern slope near the free surface, where the slope geometry is steep and joints are densely developed. The peak total displacement reaches 0.44 cm, which is within acceptable limits for natural conditions in fractured rock masses.

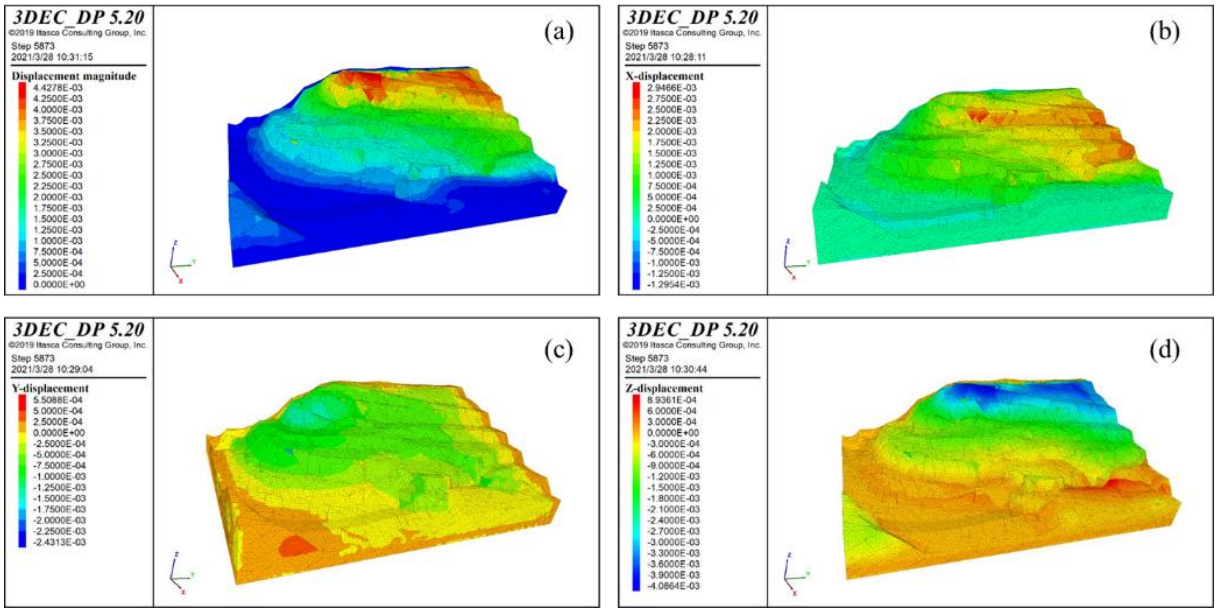

Figure 9: (a) Total displacement contour of the slope under natural conditions (DEM); (b) X-direction displacement under natural conditions; (c) Y-direction displacement under natural conditions; (d) Z-direction displacement under natural conditions.

To assess the influence of extreme weather scenarios on slope stability, heavy rainfall conditions were simulated by applying a strength reduction factor of 0.9 to the cohesion and internal friction angle of both the rock mass and structural planes. This approach, although empirical, has been widely adopted in slope engineering as a simplified and conservative approximation of rainfall-induced mechanical degradation. The simplification ensures computational efficiency and is considered reasonable for preliminary engineering evaluation. The reduction factor reflects cumulative effects such as surface softening, weakening due to increased saturation, and partial loss of matric suction.

Under simulated rainstorm conditions, the slope remains stable, with a calculated Factor of Safety (FoS) of 1.17, still exceeding the conventional safety threshold. However, a noticeable increase in displacement is observed across multiple directions, indicating a reduction in overall stiffness and an increased tendency for localized deformation. Figures 10 shows the displacement cloud maps under rainstorm conditions.The maximum total displacement reaches 0.60 cm, primarily concentrated in the upper eastern slope zone, where the combination of steep geometry, high joint connectivity (notably the J2 and J3 sets), and exposed free face contributes to deformation amplification. In the X-direction, displacement increases to 0.38 cm, particularly along steeply dipping joint-controlled surfaces. This is indicative of enhanced shear activation along pre-existing fissures, suggesting the potential for progressive sliding initiation in structurally weakened zones. In the Y-direction, the maximum displacement reaches -0.43 cm, highlighting lateral expansion and deformation of the southern slope sector. This trend may be associated with joint dilation or block rearrangement facilitated by moisture-induced loss of

interlocking friction. In the Z-direction, a maximum settlement of -0.43 cm is observed at the slope crest and upper edge, implying gravity-driven vertical compaction, joint closure, and minor block detachment near the slope surface. These displacement patterns reflect a more active deformation regime compared to dry conditions, though not yet indicative of global instability. The areas of concentration—particularly at the upper eastern slope—suggest that under prolonged or repeated rainfall events, failure could evolve through a combination of progressive shear-slip and top-down block disintegration.

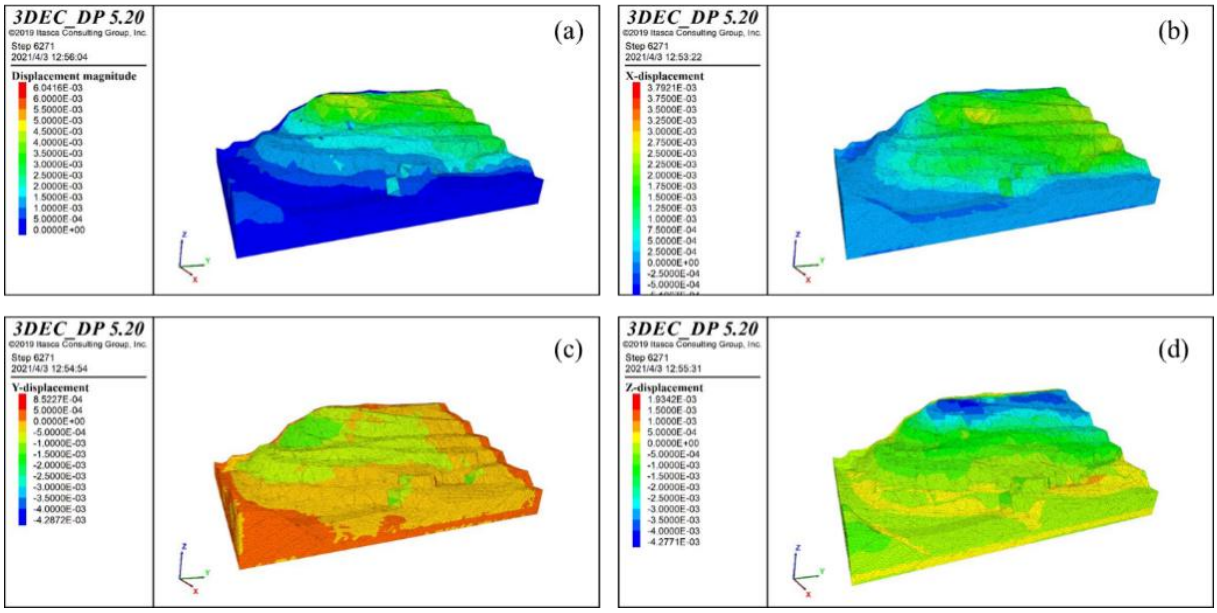

Figure 10: (a) Total displacement contour of the slope under rainstorm conditions (DEM); (b) X-direction displacement under natural conditions; (c) Y-direction displacement under natural conditions; (d) Z-direction displacement under natural conditions.

4.3 Finite Difference Numerical Simulation Analysis

In the finite difference method (FDM) simulation, the rock mass is treated as a continuous, homogeneous, and isotropic medium at the macroscopic scale, despite the presence of discontinuities such as joints and micro-fractures. This homogenization is achieved by incorporating the mechanical effects of structural defects into equivalent continuum parameters, such as reduced elastic modulus and adjusted strength indices. When available, parameter values were derived from laboratory tests; otherwise, conservative estimates were adopted based on rock mass classification schemes, including the Geological Strength Index (GSI) and relevant empirical correlations. The material properties used for the FDM model are also listed in Table 8.

Figure 11 illustrates the displacement cloud maps of the slope under natural (dry) conditions simulated using FDM. The results show that the slope maintains good stability, with a calculated Factor of Safety (FoS) of 1.86, significantly above the critical threshold of 1.3 commonly used in design. This high safety margin reflects the relatively conservative parameter selection and the absence of unfavorable external loads such as rainfall infiltration or seismic excitation. Displacement within the model is concentrated near the slope crest and the upper surface of the eastern slope, consistent with zones of reduced confining pressure and geometric convexity. The maximum total displacement is 0.295 cm, primarily manifested as vertical settlement. This settlement is attributed to gravity-driven compaction of the upper slope, where the overburden stress is relatively low and structural defects accumulate. The X-direction displacement is

localized at the toe of the steep upper eastern slope, reaching 0.049 cm. This minor horizontal movement likely results from stress redistribution and tensile relaxation in response to local unloading near the free face. The relatively small magnitude of this displacement may also reflect the limitation of the continuum assumption, which tends to underestimate discontinuity-induced shear deformation. In the Y-direction, the displacement is negligible, with a peak value of -0.032 cm, and no obvious concentration zones. This indicates that the slope exhibits minimal lateral deformation in the north–south direction, consistent with the overall structural orientation and stress field, which is predominantly aligned in the east–west plane. The Z-direction displacement, with a maximum of -0.295 cm, confirms settlement at the crest and slight upward rebound at the slope toe. This pattern is indicative of differential consolidation and potential stress arching effects, especially in areas where the slope base exhibits higher stiffness or confinement.

The absence of large horizontal deformation and the dominance of vertical settlement suggest that the slope under natural conditions behaves in a quasi-static equilibrium state, governed by gravitational stress and constrained by basal stiffness. The FDM results also highlight the model's tendency to smooth deformation responses, which is consistent with its assumption of a continuous medium.

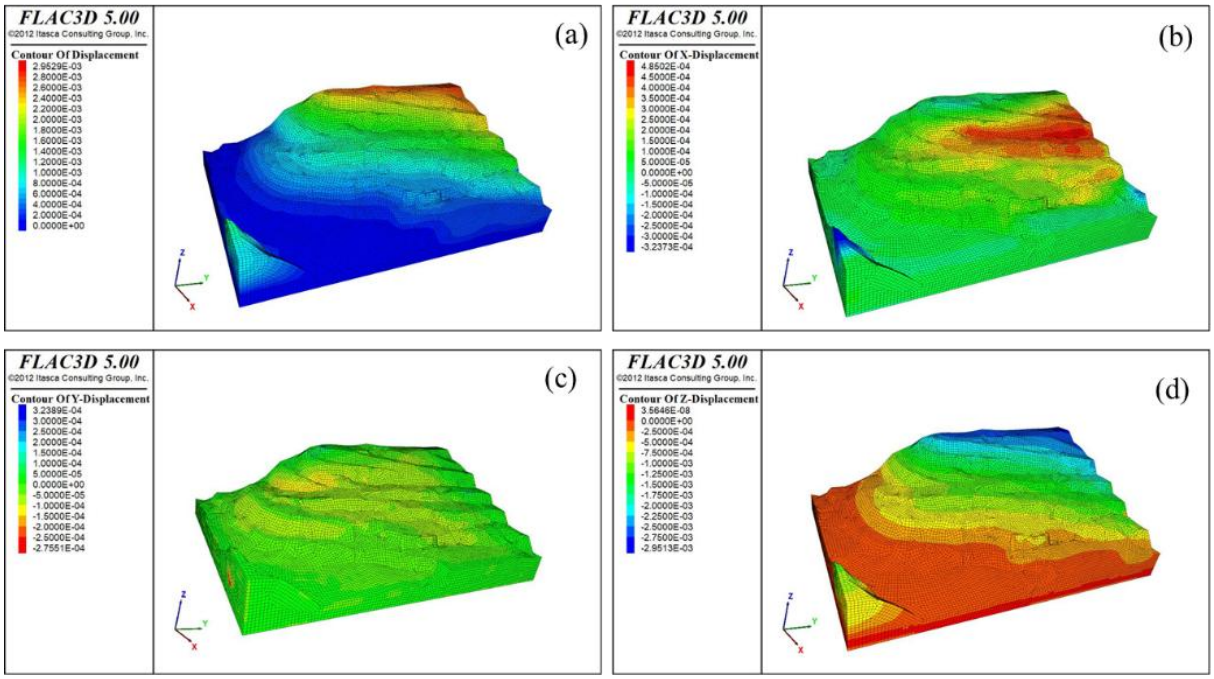

Figure 11: (a) Total displacement contour of the slope under natural conditions (FDM); (b) X-direction displacement under natural conditions; (c) Y-direction displacement under natural conditions; (d) Z-direction displacement under natural conditions.

To evaluate slope performance under extreme weather conditions, rainfall was simulated in the finite difference model by applying a reduction factor of 0.9 to the shear strength parameters (cohesion c and internal friction angle φ) of both the rock mass and the structural planes. This adjustment reflects the weakened mechanical behavior of rock materials due to increased saturation, reduced matric suction, and potential softening effects, consistent with widely adopted empirical practices in slope engineering. The strength reduction method provides a computationally efficient approximation of rainfall-induced degradation.

Figure 12 illustrate the displacement cloud maps of the slope under simulated rainstorm conditions. The overall stability of the slope remains acceptable, with a computed Factor of

Safety (FoS) of 1.52, indicating that the slope is still within a stable range but with a reduced safety margin compared to the dry condition (FoS = 1.86). This reduction confirms that rainfall infiltration substantially diminishes slope resistance, especially in fractured rock masses with pre-existing joints. The maximum total displacement increases to 0.32 cm, primarily located at the upper eastern slope, which coincides with zones of reduced confining stress and high joint connectivity. This spatial concentration of deformation mirrors the trend observed under dry conditions but exhibits enhanced magnitude and extent. In the X-direction, displacement increases to 0.058 cm, with values concentrated near the toe of the steep upper slope on the eastern side. This displacement likely results from shear mobilization along subvertical joints. Under saturated conditions, the effective friction reduces, leading to more active joint slip. The Y-direction displacement reaches -0.042 cm, still relatively minor and without clear concentration zones. However, compared to dry conditions, the increase suggests slight lateral expansion, possibly caused by block dilation and loosening due to moisture absorption. In the Z-direction, a maximum settlement of -0.316 cm is observed at the crest and upper slope region, coupled with minor uplift at the slope toe, a deformation mode indicative of gravitational consolidation and arching effects within the slope mass. Compared to natural conditions, the increased vertical deformation indicates that saturation reduces inter-particle stiffness and increases compressibility of the rock mass. The comparison with dry conditions highlights that rainfall primarily affects the vertical and shear deformation mechanisms, while lateral deformation remains limited. The increase in vertical settlement and horizontal shear, particularly near steep joints, suggests that under prolonged or repeated rainfall events, progressive failure may initiate from the upper slope and evolve downward.

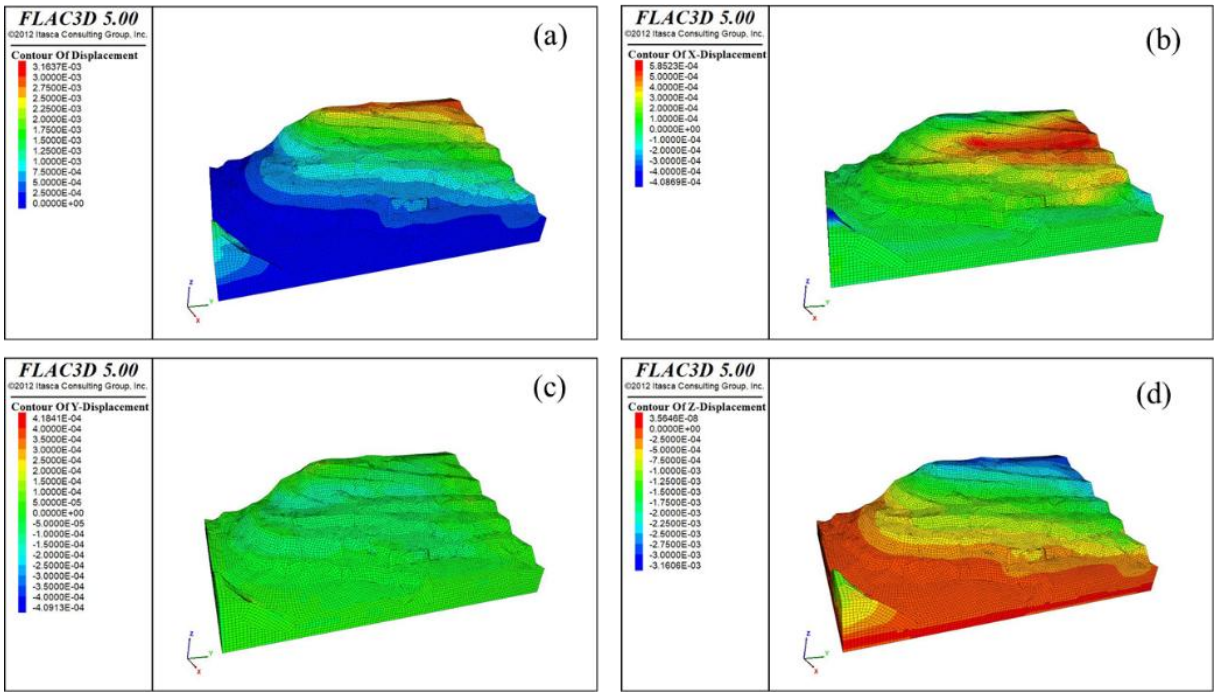

Figure 12: (a) Total displacement contour of the slope under rainstorm conditions (FDM); (b) X-direction displacement under natural conditions; (c) Y-direction displacement under natural conditions; (d) Z-direction displacement under natural conditions.

4.4 Comparative Analysis Between DEM and FDM

To better understand the mechanical behavior and failure mechanisms of the slope, both the Discrete Element Method (DEM) and the Finite Difference Method (FDM) were used for

numerical simulation. Table 9 summarizes the computed displacement and Factor of Safety (FoS) under natural and rainstorm conditions using both methods.

Table 9: Comparison between DEM and FDM

Working conditions	Finite difference simulation		Discrete element simulation	
	Natural conditions	rainstorm conditions	Natural conditions	rainstorm conditions
Stability factor	1.86	1.52	1.33	1.17
Stability analysis	Stability	Stability	Stability	Stability
X_{Max} displacement (cm)	0.049	0.06	0.29	0.38
Y_{Max} displacement (cm)	-0.03	-0.04	-0.24	-0.43
Z_{Max} displacement (cm)	-0.295	-0.32	-0.41	-0.43

On the one hand, from a qualitative perspective, both numerical approaches identify the slope as stable under the two loading scenarios. However, significant differences emerge in terms of FoS values and deformation modes, owing to their fundamentally distinct modeling philosophies. Specifically, the DEM model implemented in 3DEC considers the explicit discontinuity of rock masses, including joints and block interactions. As a result, the calculated FoS is consistently lower than that obtained from FDM, reflecting a more conservative estimate of slope stability. In contrast, the FDM assumes the rock mass to be a continuum medium with homogenized properties, which may overestimate stiffness and strength, particularly in jointed rock slopes. On the other hand, from a quantitative standpoint, the DEM results exhibit larger total and directional displacements, particularly under adverse (rainstorm) conditions. Horizontal displacement components (especially in the X-direction) are more prominent in the DEM results, attributed to joint sliding and inter-block movement, which are not captured in the continuum-based FDM. In FDM, deformation is predominantly vertical, primarily due to creep-like settlement at the slope crest.

These contrasting deformation patterns are reflected in the unbalanced force evolution curves (Figure 13). The FDM displays a smooth, low-magnitude curve with rapid convergence, indicating a relatively stable and gradual equilibrium process. Conversely, the DEM records larger, high-frequency fluctuations, associated with localized slip events, joint dilation, and micro-instabilities, which reflect progressive failure and energy release during slope deformation.

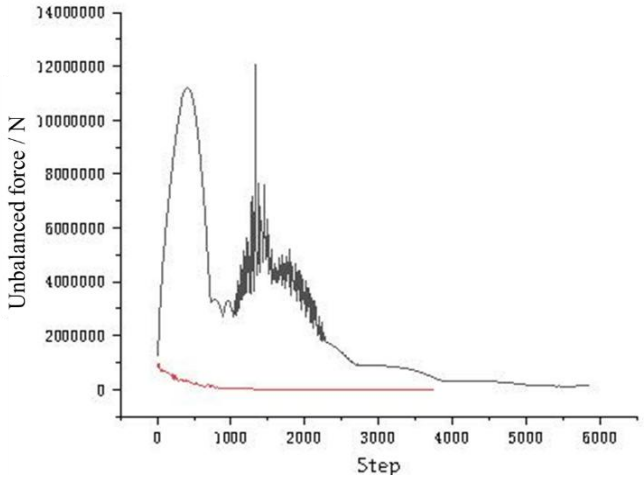

Figure 13: Comparison of the maximum unbalanced forces.

To further distinguish the failure mechanisms, strength parameters were reduced to simulate post-peak behavior. As shown in Figure 14, the FDM predicts a failure process initiated at the slope toe, followed by the upward development of a continuous plastic shear zone. This pattern results in a progressive translational landslide, characteristic of ductile deformation in homogeneous media. The final sliding surface is smooth and continuous, consistent with the assumption of strain-softening plasticity. In contrast, the DEM exhibits abrupt failure with distinct brittle characteristics. Failure initiates with the formation of tensile cracks at the slope crest, followed by the rapid coalescence of cracks and block separation. The process is marked by stepwise collapses, backward-tilting of blocks, and tensile fracture development along jointed zones. This reflects a toppling-type rock slope failure mechanism, where fracture-controlled instability dominates.

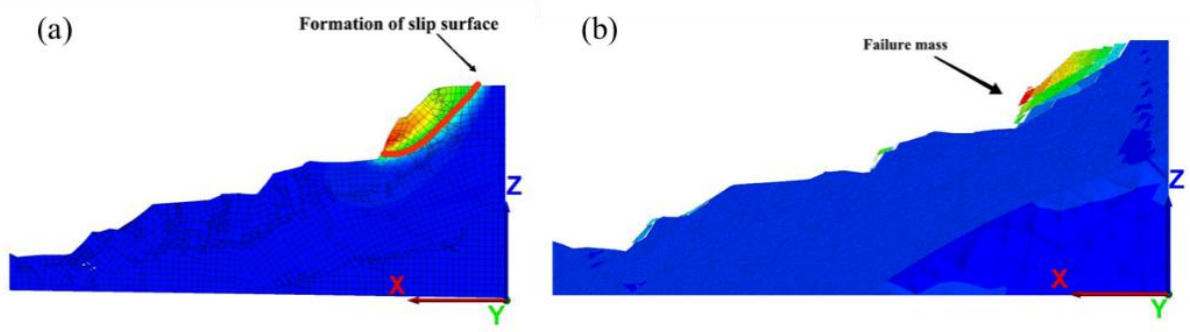

Figure 14: (a) Schematic diagram of finite difference slope failure;(b) Schematic diagram of discrete element slope failure.

In summary, the FDM is suitable for capturing large-scale deformation trends and yielding FoS estimates in relatively continuous slopes. However, it is less effective in reproducing the localized brittle failure mechanisms of jointed rock masses. In contrast, the DEM provides a more realistic representation of discontinuous rock behavior, especially under complex structural controls, but at the cost of higher computational demands and sensitivity to input parameters such as joint orientation, connectivity, and block geometry. Therefore, integrating insights from both methods provides a more comprehensive understanding of slope stability and failure processes.

5 Validation of Numerical Simulation Using Monitoring Data

To assess the reliability of the numerical simulations, displacement data from three monitoring points located on the western slope were compared with the corresponding results obtained from both the Discrete Element Method (DEM) and the Finite Difference Method (FDM). These monitoring points were strategically placed at the slope crest and within key regions of the fault fracture zone. The locations of these points are shown in Figure 15, and the corresponding field monitoring data are summarized in Table 10. In the numerical models, virtual monitoring points were set at the same locations as the field instruments. The history displacement command was used to extract the X- and Z-direction displacement histories at each point for both DEM and FDM simulations under natural (dry) conditions.

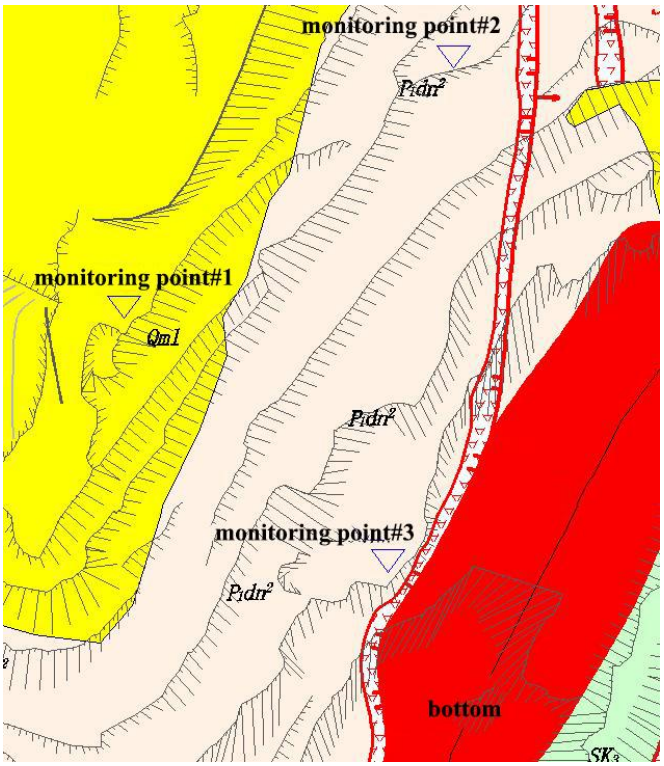

Figure 15: Locations of field monitoring points on the western slope.

Table 10: Comparison Between Numerical Simulation Results and Field Monitoring Displacements

Points Numbers	Type	X (mm)	Difference from monitoring	Deviation degree (%)	Z (mm)	Difference from monitoring	Deviation degree (%)
1 #	Monitoring points	1.45	/	/	3.01	/	/
	DEM	2.1	0.65	45%	3.4	0.39	13%
	FDM	0.19	-1.26	87%	1.74	-1.27	42%
2 #	Monitoring points	2.94	/	/	3.23	/	/
	DEM	4.0	0.74	27%	4.2	0.97	30%
	FDM	0.28	-2.98	90%	1.1	-2.13	66%
3 #	Monitoring points	0.6	/	/	0.4	/	/
	DEM	0.8	0.2	33%	0.5	0.1	25%
	FDM	0.15	-0.45	75%	0.5	0.1	25%

5.1 Comparison with Finite Difference Method Results

As shown in Figure 16, the displacement-time histories from the FDM model revealed rapid convergence toward steady-state values for all three monitoring points. This is consistent with a stable slope condition under self-weight loading, as also indicated by the computed factor of safety (FoS > 1.80). The recorded displacements were:

Monitoring Point 1: X = 0.19 mm, Z = 1.74 mm;

Monitoring Point 2: X = 0.28 mm, Z = 1.10 mm;

Monitoring Point 3: X = 0.15 mm, Z = 0.50 mm.

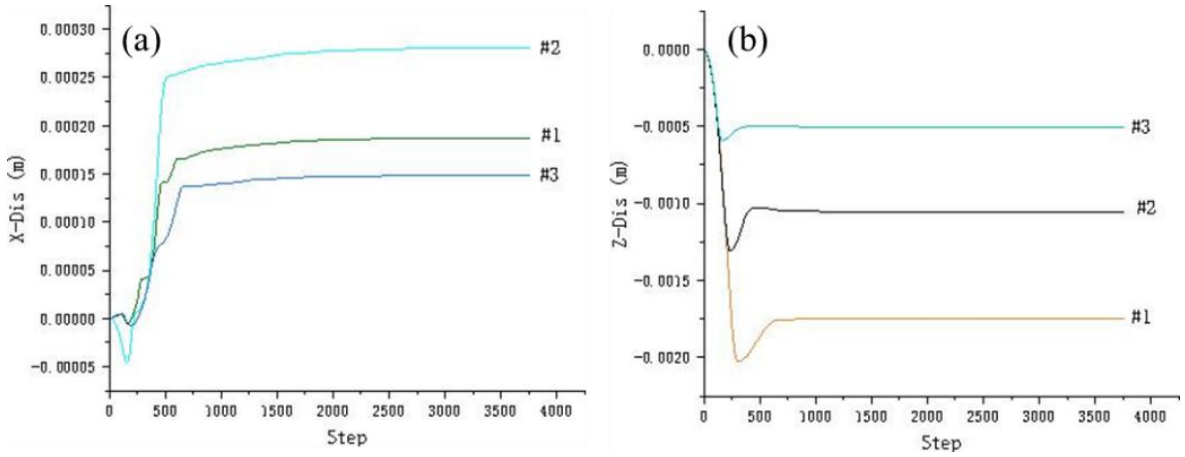

Figure 16: (a) Displacement-Time Curves of FDM Simulated Monitoring Points in X Directions; (b) Displacement-Time Curves of FDM Simulated Monitoring Points in Z Directions.

A comparison with field data (Table 10) shows good agreement in Z-direction displacements but significant underestimation in the X direction. Specifically, the horizontal displacement error ranges between 75% and 90%, while the vertical displacement deviation ranges between 25% and 66%. This discrepancy is likely due to the homogenized treatment of the rock mass in FDM, which does not explicitly account for the slip and deformation along structural planes.Moreover, FDM simulations lack the capacity to capture stress redistribution caused by progressive failure along discontinuities. As a result, it tends to underpredict displacement in structurally controlled failure modes, especially in regions influenced by shearing and fault slip.

5.2 Comparison with Discrete Element Method Results

The DEM results, illustrated in Figure 17, also showed a fast convergence of displacement values, indicating mechanical equilibrium. The final stabilized displacements were:

Monitoring Point 1: X = 2.1 mm, Z = 3.4 mm;
Monitoring Point 2: X = 4.0 mm, Z = 4.2 mm;
Monitoring Point 3: X = 0.8 mm, Z = 0.5 mm.

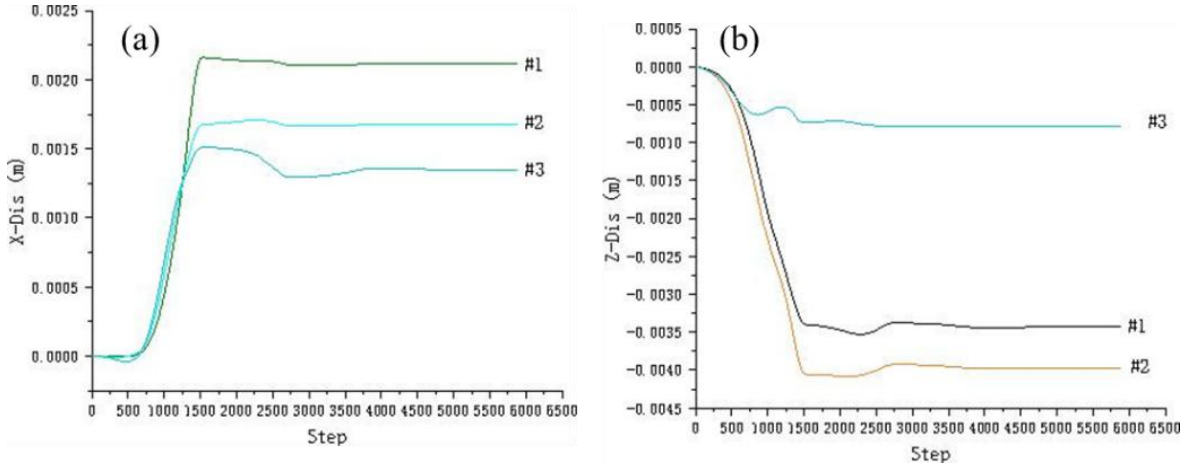

Figure 17: (a) Displacement-time curves of DEM simulated monitoring points in X directions; (b) Displacement-time curves of DEM simulated monitoring points in Z directions.

These values show improved consistency with actual monitoring records, with X-direction errors ranging from 27% to 45%, and Z-direction errors ranging from 13% to 30%. The improved performance of the DEM model may be attributed to its ability to explicitly represent structural discontinuities such as joints and faults, which are critical in controlling the deformation of fractured rock slopes. Furthermore, DEM can simulate brittle failure modes and complex fracture propagation paths, which were observed in field inspections. This makes it particularly suitable for modeling mechanically anisotropic and discontinuous media.

5.3 Summary and Discussion

A side-by-side comparison of monitoring data and numerical simulation outputs is presented in Table 10. In general:

FDM effectively captures global deformation trends, especially vertical settlement under gravity, but fails to represent joint-induced horizontal displacement, resulting in large deviations in lateral deformation estimates. DEM provides a more accurate match to field observations, especially in reproducing localized displacements along structurally weak zones. This contrast reflects fundamental modeling differences: FDM assumes a continuous, homogeneous equivalent medium, suitable for soils or massive rocks, while DEM accommodates the discrete and heterogeneous nature of fractured rock masses.

From an engineering perspective, these findings underscore the need for model selection based on geological conditions: For intact or mildly fractured slopes, FDM offers a computationally efficient tool with reasonable accuracy. For heavily jointed, faulted, or blocky rock slopes, DEM is preferable due to its capacity to simulate discontinuity-controlled deformation and failure.

It should also be noted that the calibration of DEM input parameters, such as joint stiffness and strength, remains a critical challenge, often requiring extensive laboratory and field data. Moreover, computational cost and time are higher in DEM simulations, which may limit their use in routine slope design but are justified in high-risk or high-value projects. In conclusion, while both methods have their strengths and limitations, DEM exhibits superior predictive capability in jointed rock environments, and its validation against monitoring data enhances confidence in its use for detailed stability assessment and failure prediction.

6 Conclusions

The numerical analyses using both the Discrete Element Method (DEM) and Finite Difference Method (FDM) indicate that the studied slope remains stable under both natural and rainstorm conditions, with Factors of Safety (FoS) exceeding common design thresholds. However, DEM results generally show lower FoS values and larger displacements, reflecting its greater sensitivity to structural discontinuities and localized deformation mechanisms, while FDM tends to provide more conservative deformation estimates for continuous media.

Differences in predicted deformation patterns and failure mechanisms are observed between the two approaches. The FDM simulation suggests a progressive, toe-initiated shear failure typical of ductile behavior in equivalent continua, whereas the DEM captures brittle failure features such as tensile cracking, wedge separation, and stepwise block disintegration. These results suggest that the DEM may offer more detailed insights into failure processes in structurally complex rock slopes.

Comparison with field monitoring data shows that the DEM achieves better agreement with observed displacements, particularly in the horizontal direction. While the FDM captures the general trend of vertical settlement, it tends to underestimate shear and lateral movements,

likely due to its continuum assumptions. This highlights the importance of method selection based on the geological and structural complexity of the slope.

Overall, the DEM demonstrates advantages in modeling the mechanical response of jointed rock masses, especially where failure is governed by discontinuities. While it involves greater computational effort and parameter calibration, it may be more suitable for high-resolution analysis of structurally controlled slope stability. The FDM, with its lower computational demands and robust convergence, remains useful for preliminary evaluations or slopes with relatively homogeneous and massive rock conditions.

Data availability

The datasets generated during and/or analyzed during the current study are available from the corresponding author on reasonable request.

Acknowledgements

We gratefully acknowledge financial support from the National Natural Science Foundation of China (NSFC) (Grant No. 41861134008). The authors are also grateful to the anonymous reviewers for their many helpful comments, which have greatly improved this paper.

CRediT authorship contribution statement

Qianzhou Rong: Conceptualization, Data Curation, Formal analysis, Writing–original draft. **Shiguang Xu**: Conceptualization, Visualization, Writing–review & editing. **Yi Yang**: Visualization, Writing–review & editing. **Lichun He**: Conceptualization, Formal analysis.

Declaration of competing interest

The authors declare that they have no known competing financial interests or personal relationships that could have appeared to influence the work reported in this paper.

Funding

We gratefully acknowledge financial support from the National Natural Science Foundation of China (NSFC) (Grant No. 41861134008).

References

[1] Rezaei, M., & Seyed Mousavi, S. Z. (2024). Slope stability analysis of an open pit mine with considering the weathering agent: Field, laboratory and numerical studies. Engineering Geology, 333, 107503.

[2] Nata, R. A., Ren, G., Ge, Y., & Pradhana, A. (2025). Designing stable rock slopes in open-pit mines: A case study of andesite mining at Anugerah Berkah Sejahtera. Sustainability, 17(13), 5711.

[3] Haundi, T., & Okonta, F. (2025). A systematic review of physical modelling techniques, developments and applications in slope stability analyses. Indian Geotechnical Journal, 55, 994-1016.

[4] Chen, Q., Yang, Y. C., Zhu, Q. Y., Li, H. B., Yang, X. G., & Zhou, J. W. (2025). Three-dimensional jointed rock slope stability analysis using integrated block theory and DFN-DEM modeling. Computers and Geotechnics, 184, 107549.

[5] An, H. M., Fan, Y. Q., Liu, H. Y., Zhou, J. W., & Zhang, L. (2022). The state of the art and new insight into combined finite-discrete element modelling of the entire rock slope failure process. Sustainability, 14(9), 4896.

[6] Zhou, Z., Gao, T., Sun, J., Gao, C., Bai, S., Jin, G., & Liu, Y. (2024). An FDM-DEM coupling method based on REV for stability analysis of tunnel surrounding rock. Tunnelling and Underground Space Technology, 152, 105917.

[7] Jiang, M., & Murakami, A. (2012). Distinct element method analyses of idealized bonded-granulate cut slope. Granular Matter, 14, 393-410.

[8] Antolini, F., Barla, M., Gigli, G., Giorgetti, A., & Casagli, N. (2016). Combined finite-discrete numerical modeling of runout of the Torgiovannetto di Assisi rockslide in central Italy. International Journal of Geomechanics, 16(6), 04016019.

[9] ISRM. (1986). Suggested methods for rock characterization, testing and monitoring. Pergamon Press.

[10] Hoek, E., & Brown, E. T. (1997). Practical estimates of rock mass strength. International Journal of Rock Mechanics and Mining Sciences, 34(8), 1165-1186.

[11] Hoek, E., Carranza-Torres, C., & Corkum, B. (2002). Hoek-Brown failure criterion: 2002 edition. Proceedings of NARMS-TAC, 1(1), 267-273.

[12] Bandis, S., Lumsden, A. C., & Barton, N. R. (1983). Fundamentals of rock joint deformation. International Journal of Rock Mechanics and Mining Sciences & Geomechanics Abstracts, 20(6), 249-268.

[13] Barton, N. (1973). Review of a new shear-strength criterion for rock joints. Engineering Geology, 7(4), 287-332.

[14] Tse, R., & Cruden, D. M. (1979). Estimating joint roughness coefficients. International Journal of Rock Mechanics and Mining Sciences, 16(5), 303-307.

[15] Yau, J. S., Lee, C. F., & Tang, H. Y. (1987). Automated estimation of joint roughness coefficient (JRC) using digital image processing. Rock Mechanics and Rock Engineering, 20(2), 87-106.

[16] Goodman, R. E. (1976). Methods of geological engineering in discontinuous rocks. West Publishing.

[17] Barton, N., & Choubey, V. (1977). The shear strength of rock joints in theory and practice. Rock Mechanics, 10, 1-54.